Submesoscale CO_2 variability across an upwelling front off Peru

Eike E. Köhn[1], Sören Thomsen[1], Damian L. Arévalo-Martínez[1], and Torsten Kanzow[2]

[1]GEOMAR Helmholtz Centre for Ocean Research Kiel, Kiel, Germany
[2]Alfred-Wegener-Institute Helmholtz Centre for Polar and Marine Research, Bremerhaven, Germany

Correspondence to: Eike E. Köhn (ekoehn@geomar.de)

Abstract. While being a major source for atmospheric CO_2, the Peruvian upwelling region exhibits strong variability in surface fCO$_2$ on short spatial and temporal scales. Understanding the physical processes driving the strong variability is of fundamental importance for constraining the effect of marine emissions from upwelling regions on the global CO_2 budget. In this study, a frontal decay on length scales of $\mathcal{O}(10 \text{ km})$ was observed off the Peruvian coast following a pronounced
5   decrease in downfrontal (equatorward) wind speed with a time lag of 9 hours. Simultaneously, the sea-to-air flux of CO_2 on the inshore (cold) side of the front dropped from up to 80 to 10 $\text{mmol m}^{-2} \text{ day}^{-1}$, while the offshore (warm) side of the front was constantly outgassing at a rate of 10-20 $\text{mmol m}^{-2} \text{ day}^{-1}$. Based on repeated ship transects the decay of the front was observed to occur in two phases. The first phase was characterized by a development of coherent surface temperature anomalies which gained in amplitude over 6-9 hours. The second phase was characterized by a disappearance of the surface
10   temperature front within 6 hours. Submesoscale mixed layer instabilities were present but seem too slow to completely remove the temperature gradient in this short time period. Dynamics such as a pressure driven gravity current appear to be a likely mechanism behind the evolution of the front.

1   Introduction

Although the ocean generally acts as a net sink for atmospheric CO_2 (Takahashi et al., 2009), most low latitude eastern bound-
15   ary upwelling systems (EBUS) are natural sources of CO_2 to the atmosphere (Chavez et al., 2007; Capone and Hutchins, 2013; Gruber, 2015). The distribution of CO_2 in such areas is complex and results from the interaction betweeen cooling/warming at the surface, upwelling and mixing, biological activity, and riverine carbon and nutrient input (Laruelle et al., 2014; Gruber, 2015). As one of the four major EBUS, the Peruvian upwelling region is an important area for the exchange of climate relevant gases (e.g. CO_2, N_2O) between the ocean and the atmosphere (Friederich et al., 2008; Arévalo-Martínez et al., 2015). Hence,
20   quantification of sea-to-air fluxes of CO_2 as well as their spatial and temporal variability in the Peruvian upwelling region is essential for constraining the global budget of CO_2 in a changing climate.

High variability of surface CO_2 in the Peruvian upwelling region is observed on short time $\mathcal{O}$(hours-days) and space $\mathcal{O}$(km) scales driven by both biological and physical processes (Friederich et al., 2008). The sharp lateral temperature gradient, separating the newly upwelled, cold water from warm surface waters further offshore, allows for pronounced frontal processes, which manifest themselves in eddies and filaments (Penven et al., 2005; Chaigneau et al., 2008; McWilliams et al., 2009;
25   Colas et al., 2012; Thomsen et al., 2016a). These submesoscale features, which go along with Rossby numbers $Ro = \mathcal{O}(1)$,

can develop strong vertical velocities in the upper ocean layer. Thus, surface fronts may enable the exchange of large amounts of heat and gas between the atmosphere and the subsurface ocean (Ferrari, 2011). However, submesoscale frontal processes are difficult to observe due to their small spatial and temporal scales. At the same time the importance of these dynamics for physical-biogeochemical coupling has been put forward by model studies, e.g. by altering the vertical transports of nutrients and organic carbon (Lapeyre and Klein, 2006; Lévy et al., 2012).

The link between the surface CO_2 distribution and the (sub-) mesoscale flow field was studied in the open ocean of the Northeast Atlantic by Merlivat et al. (2009), using both underway and lagrangian surface drifter measurements. During the measurement period, the study area was characterized by weak eddy kinetic energy. Still, submesoscale variability with large amplitude variations of surface CO_2 concentrations on horizontal length scales of $\mathcal{O}(10 \text{ km})$ was observed. This variability was successfully reproduced by the modelling study of Resplandy et al. (2009) but it does not seem to have a major effect on the model's overall CO_2 budget. The influence of submesoscale variability on the overall CO_2 budget might be stronger in the case of EBUS due to the ubiquitous existence of sharp fronts and filaments, i.e. in the case of a highly energetic (sub-) mesoscale flow field (McWilliams et al., 2009; Colas et al., 2012). However, so far no observations are available which describe the variability on the submesoscale off Peru.

In this study repeated measurements of CO_2 and physical properties across the upwelling front off Peru near $14°$ S are presented (see Fig. 1 for the large scale setting of the experiment). Throughout the two day experiment, we observed short-term fluctuations (timescales on $\mathcal{O}(\text{hours})$) of the surface temperature and velocity field. Simultaneously, surface CO_2 sea-to-air fluxes showed pronounced changes, implicating the importance of these timescales for the ocean-atmosphere gas exchange. The goal of this paper are to: 1) document the high-frequency variability across the upwelling front and 2) discuss possible physical driving mechanisms, improving our current understanding of the variability of surface CO_2 in the Peruvian upwelling region.

This paper is structured as follows: In section 2 we present the experiment, the physical and biogeochemical datasets used for this study, as well as the methods employed for their analysis. Section 3 contains a description of the initial state of the front. Observations from the following frontal evolution are presented in section 4. Subsequently, the changes across the temperature front are analyzed in the context of various possible underlying dynamics, such as surface heating (Section 4.1), Ekman buoyancy fluxes (Section 4.2), submesoscale mixed layer instabilities (Section 4.3) or pressure driven gravity currents (Section 4.4). In section 5 these mechanisms are compared with respect to their associated buoyancy fluxes. Section 6 contains a discussion of the different mechanisms which possibly drive the observed variability. The conclusions drawn from this study follow in section 7.

2 Data and methods

2.1 Hydrographic and meteorological measurements

Near $14°$ S and $76°30'$ W the Peruvian upwelling region is characterized by a strong (quasi-) permanent upwelling cell (Fig. 1). The corresponding "upwelling front" was intensively sampled from February 16 to 18 during the RV *Meteor* cruise M93
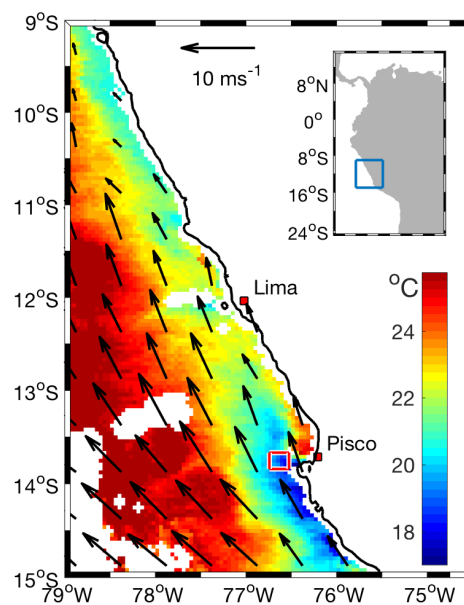
Figure 1. MODIS SST (color) and ASCAT (Advanced Scatterometer) wind field (arrows) off the Peruvian coast on February 16, 2013. The small red box shows the study region off Pisco.

in February/March 2013. The field work was carried out within the framework of the Collaborative Research Centre SFB754 "Climate-Biogeochemistry Interactions in the Tropical Ocean" (www.sfb754.de). The experiment's procedure was as follows: Prior to the main experiment, a CTD section (transect "A", black squares in Fig. 2) was conducted on February 16 from 10:00 to 15:00 (time always in UTC unless stated differently) to document the horizontal circulation and the initial vertical distribution of temperature, salinity, dissolved oxygen (O_2) and chlorophyll-a (Chl-*a*) across the front. Starting on February 17 at 04:00, the upwelling front was mapped by seven ∼10 km long zonal transects. These were conducted from north to south in 1.8 km spacing (Fig. 2). Each zonal transect took about 45 minutes. From the highest and lowest surface temperature recorded, a cross-frontal axis was estimated. Subsequently, 17 cross-frontal transects were conducted along this axis to study the variability of the front on timescales of several hours. Among these, two high-resolution temperature sections "B" and "C" were conducted as cross-frontal transects 12 and 14. The high-resolution transects took 4.5 hours each to complete, while a regular cross-frontal transect was completed in 40 minutes. The cross-frontal transects were conducted within a 1.8 km wide corridor on three parallel tracks (Fig. 2).

The physical state of the upwelling front is mainly deduced from underway temperature, wind and velocity measurements. Underway temperature was measured by the thermosalinograph using an external SBE-38 digital thermometer at 3.5 - 4 m depth at the vessel's port-side bow. Temperature data was gathered at 0.1 Hz and filtered by a 2nd order lowpass butterworth filter with a cutoff period of 250 seconds to remove the effect due to high frequent ship movements. Wind velocity and direction
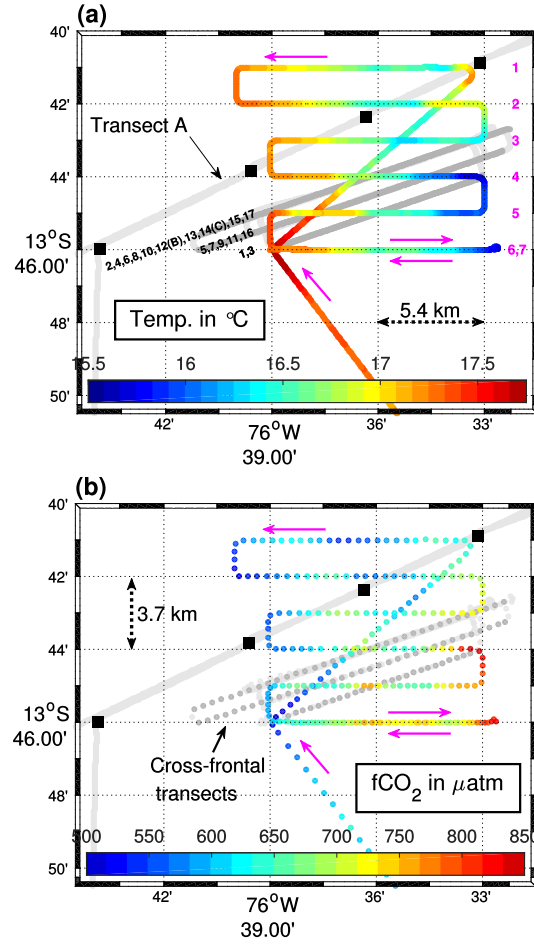
3

Figure 2. Sampling map of underway temperature (a) and $f\text{CO}_2$ (b) along the cruise track. The solid light grey line shows the CTD section (transect A) conducted prior to the seven zonal transects, with black squares indicating CTD stations. The 17 cross-frontal transects are marked by the dark grey lines (a) and dots (b). The black numbers in (a) correspond to the cross-frontal transects. Transects 12 and 14 correspond to the high-resolution subsurface temperature transects B and C. Magenta arrows show the direction of the ship's track and magenta numbers label the zonal transects. The area presented in both panels is depicted as a red square in Fig. 1.

were measured at a height of 35.3 m above the sea surface at a temporal resolution of 60 seconds. The surface wind stress was estimated from these measurements following Smith (1988). Underway ocean current velocity measurements with a vertical resolution of 4 m were obtained from a vessel-mounted 75 kHz ADCP (vmADCP). The shallowest vmADCP based current velocities were obtained in a bin centered at 11 m below the sea surface. The data was averaged in 1-minute-ensembles and

5 smoothed using a 3-minute running mean. A $16.56°$ counterclockwise rotation is applied to transform the measured currents into along-front and cross-front velocities (note the frontal orientation in Fig. 2). As a result positive cross-front velocities are directed towards the coast and positive along-front velocities indicate an equatorward flow. Underway measurements of salinity

are unavailable as the thermosalinograph's conductivity sensor failed to produce consistent results. Likewise, temperature and vmADCP measurements taken during periods of highly variable vessel speed and heading proved to be unreliable due to the influence of the ship. Thus, current measurements immediately before and after CTD stations are neglected in the following data analysis. During the analyzed transects the vessel speed was held at approximately constant $4 \, \text{m s}^{-1}$ in order to achieve high quality ADCP data.

Hydrographic data *below* the surface were obtained from lowered conductivity, temperature and pressure (CTD) measurements. These are arranged in transect "A" consisting of four shallow CTD profiles located 7 km apart (black squares in Fig. 2). The CTD was equipped with a fluorometer and an oxygen sensor, allowing for Chl-*a* and O_2 measurements. A detailed description of the data processing, inluding the calibration of oxygen can be found in Thomsen et al. (2016b). As the Chl-*a* concentrations measured by the WET Labs (USA) fluorometer did not differ significantly from Chl-*a* concentrations determined from water samples (Meyer et al., 2017), no further calibration than the in-factory calibration was applied to the fluorometer data (see Loginova et al. (2016) for details). In order to obtain further subsurface hydrographic information, 53 temperature profiles organized in the two cross-frontal transects B and C with a horizontal resolution of 0.3 - 0.5 km were measured using the CTD sensors mounted on a microstructure profiler. During these measurements the speed of the vessel was reduced to about $0.75 \, \text{m s}^{-1}$.

Surface diabatic heating was calculated from underway measurements as $Q_{net} = Q_{lw} + Q_{sw} + Q_{sh} + Q_{lh}$, i.e. the sum of longwave and shortwave radiation as well as sensible and latent heat fluxes. Net shortwave radiation into the ocean was estimated using underway measurements of downward shortwave radiation under consideration of the surface albedo effect (Payne, 1972). Net longwave radiation into the ocean was calculated as the difference between the measured downward longwave radiation and outgoing longwave radiation estimated using Stefan-Boltzman's law (with an emissivity of 0.985) applied to the thermosalinograph's temperature measurements. Latent and sensible heat fluxes along the cruise track were calculated using bulk formulae including the Webb-correction to the latent heat flux (Fairall et al., 1996b). During the experiment an average flux of latent heat of $20 \, \text{W m}^{-2}$ *into* the ocean was observed. This coincided with high relative humidity and partially foggy conditions. Neither a cool skin nor a warm skin correction is applied to the thermosalinograph's temperature measurements. A cool-skin would primarily form during night time, but is estimated to be on average less than 0.02 K cooler than the temperature measured by the thermosalinograph (Fairall et al., 1996a). A potentially larger warm-skin correction, which would increase outgoing longwave radiation mainly during periods of strong insolation, is not applied. This error in heatflux is however small compared to the dominant heatflux related to shortwave radiation during daytime.

The large scale sea surface temperature (SST) was retrieved from NASA's OceanColor project as daily satellite MODIS Aqua und Terra SST data (https://oceancolor.gsfc.nasa.gov/). For the large scale wind field Advanced Scatterometer (ASCAT) wind data (Bentamy and Fillon, 2012) was taken from the Asia-Pacifc Data-Research Center at the University of Hawai'i (http://apdrc.soest.hawaii.edu/datadoc/ascat.php). The spatial resolution of SST was 4 km, while the wind data was available on a $0.25°$ grid. The ubiquitous presence of clouds during the main experiment period hindered an extensive use of remote sensing datasets.

2.2 Underway CO$_2$ measurements

CO$_2$ measurements were conducted by means of an underway system as described in Arévalo-Martínez et al. (2013). Seawater was drawn on board from a depth of about 6 m by means of a LOWARA submersible pump which was installed at the ship's moonpool. Atmospheric measurements were carried out every six hours by means of an AirCadet pump (Thermoscientific Inc., USA) which continuously brought air from 35 m height into the laboratory. Likewise, control measurements of standard gas mixtures with 201.0 and 602.4 ppm CO$_2$ were used in order to post-correct our data due to instrumental drift. The gas standards were prepared at Deuste Steininger GmbH (Mühlhausen, Germany) and were calibrated at the Max Planck Institute for Biogeochemistry (Jena, Germany) against the World Meteorological Organization standard scale. CO$_2$ data calibration as well as computation of CO$_2$ fugacities (fCO$_2$) was done according to the guidelines from Dickson et al. (2007). We report all seawater and atmospheric CO$_2$ values as 1-minute means. For this, we used a mean surface salinity from all CTD measurements of the M93 campaign (35.04), as salinity was not available from underway measurements. A change in the mean salinity by 1 leads to a mean offset of 0.0055 μatm and has thus a small influence compared to temperature with an isochemical dependence of 15 μatm per °C (e.g. Körtzinger et al. (2000); Pierrot et al. (2009)). The uncertainty of the CO$_2$ measurements was hence about +/- 2 μatm. The air-sea flux of CO$_2$ was computed by using $F = kK_0(f\mathrm{CO}_{2\mathrm{sw}} - f\mathrm{CO}_{2\mathrm{air}})$, where k is the air-sea gas exchange coefficient, calculated using the parameterization of Nightingale et al. (2000) with wind speeds standardized to 10 m height (Smith, 1988). K_0 is the solubility of CO$_2$ in seawater, calculated with the equations and coefficients from Weiss (1974) and Weiss and Price (1980), and $f\mathrm{CO}_{2\mathrm{sw}}$ and $f\mathrm{CO}_{2\mathrm{air}}$ are the fugacities of CO$_2$ in seawater and atmosphere, respectively. The strongest correlation between the underway temperature and fCO$_2$ measurements was found at a time lag of 4 minutes ($r = -0.86$) (Fig. 3), which is probably due to the travel time for the seawater from the uptake to the underway CO$_2$ sensor. Thus CO$_2$ fugacities and fluxes are corrected for this time lag.

3 Physical and biogeochemical properties of the upwelling front

The experiment period can be divided into three different wind forcing regimes. The first regime is characterized by downfrontal (equatorward) winds with speeds above 10 m s^{-1} (Fig. 4). It lasts from the beginning of the experiment including the CTD transect (Fig. 5) until February 17 11:00, i.e. right after the beginning of the cross-frontal transects. During this phase, the front is characterized by a strong cross-frontal surface temperature gradient of about 1°C over 10 km (Fig. 6a). The CTD transect reveals the strong subsurface frontal signature in the temperature and salinity field (Fig. 5b,c). The mixed layer exhibits almost vertical isopycnals and is estimated to be about 15 m deep, using a $\Delta T = 0.2$ °C criterion. The southward flowing Peru Chile Undercurrent (PCUC) weakens from ~ 20 cm s^{-1} at 80 meters depth towards the surface (Fig. 5a). The along-frontal velocity is low in the shallowest ADCP bin throughout the experiment (Fig. 7). As a result, lateral along-frontal advection is likely to play a minor role at the surface. In agreement with extensive upwelling of cold, nutrient rich waters during the strong wind period the Chl-a concentrations on the onshore side of the front were strongly enhanced with concentrations reaching 7 μg l^{-1} in the mixed layer (Fig. 5e). Simultaneously, the subsurface O$_2$ minimum was drawn closer to the surface on the onshore side of the front (Fig. 5d). Concentrations below 100 μmol kg^{-1} could be found at 15 m depth and values dropped below 20 μmol
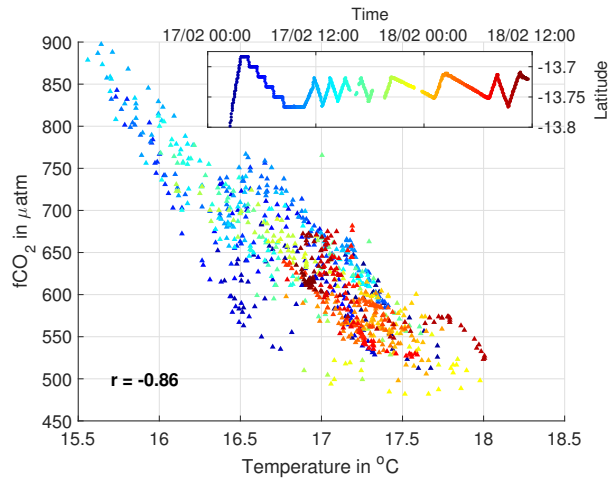
Figure 3. Correlation of surface temperature and $f\text{CO}_2$ during the main experiment. The $f\text{CO}_2$ values are corrected for a 4 minute time lag. The correlation value r is given in the bottom left corner. Data points are color-coded by their time of measurement. The top right box shows an orientation as to when the data was measured during the experiment. The color-coding carries the same information as the time axis.
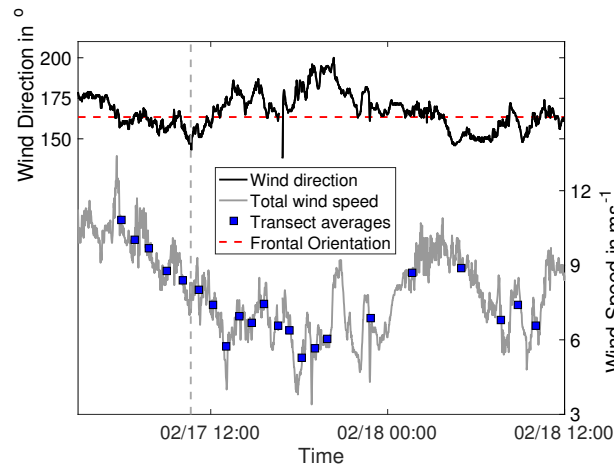

Figure 4. Time series of total wind speed (grey) and wind direction (black) from underway measurements at 35.3 m height. Blue rectangles show mean total wind speed for each zonal and cross-frontal transect. The dashed red line shows the (initial) frontal orientation deduced from the frontal mapping. The angle of 163.44° implicates the front running from south-south-east to north-north-west. The vertical dashed grey line indicates the transition from zonal to cross-frontal transects. Time is given in UTC.

kg^{-1} already beneath ~ 40 m. Further, a gradient in surface $f\text{CO}_2$ was discernible during the CTD transect (not shown) and during the zonal ship sections across the front (Fig. 2b), increasing from 600 μatm in offshore locations up to over 800 μatm on the onshore side of the front. During this period, peak sea-to-air CO_2 fluxes of over 80 $\text{mmol}\,\text{m}^{-2}\,\text{d}^{-1}$ are measured on the cold side of the front (Fig. 6d).
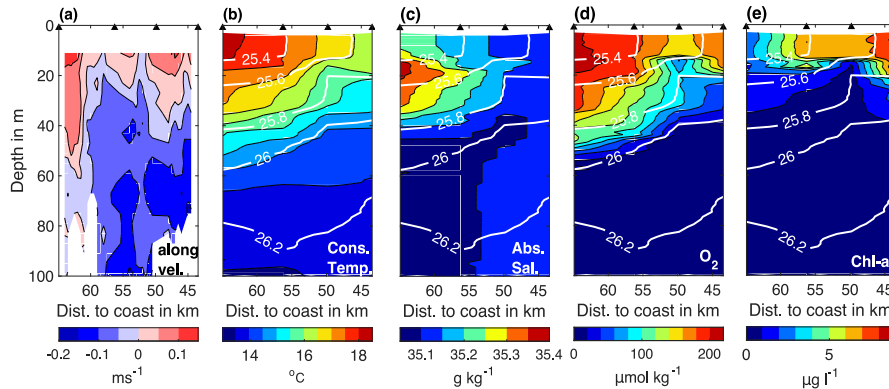
Figure 5. CTD transect across the upwelling front before the main experiment conducted on February 16, 2013. Measured quantities contain along-frontal current velocities (a), conservative temperature (b), absolute salinity (c), O_2 (d) and Chl-a concentrations (e). Isopycnals are given by white lines in (b) - (e). Around CTD stations the along-frontal velocity is horizontally linearly interpolated.

4 Cross-frontal changes after weakening of downfrontal winds

During the second wind period from 11:00 to 21:00 on February 17 the wind continues to blow in the downfrontal direction but drops to almost 5 m s^{-1} (Fig. 4). During this period the clear surface temperature gradient signal is disturbed by coherent anomalies appearing at 50 km off the coast (Fig. 6b). These anomalies grow in amplitude and lead to a break up of the clear
5   temperature gradient at around 20:00. At the same time the strong outgassing of CO_2 is reduced on the onshore side of the front (Fig. 6d), while surface fCO$_2$ values remain rather high until about 18:00 (Fig. 6c). At the beginning of the transition to the low wind speed period, a strong offshore directed velocity signal is observed close to the surface on the onshore side of the front (Fig. 7a). The velocity maximum of up to 15 cm s^{-1} deepens with increasing distance from shore. During the wind minimum, maximum offshore velocities are found at 25-30 m depth, exceeding 20 cm s^{-1} (Fig. 7c). At the same time, the
10   along-frontal velocity field exhibits a slight reduction in vertical shear (Fig. 7b,d).

    At about 21:00 on February 17 the along-frontal (equatorward) wind begins to increase again and reaches about 9 m s^{-1}, defining the beginning of the third wind regime. Initially, the surface temperature gradient vanishes and even reverses slightly, before strengthening again towards February 18 09:00. Both high-resolution temperature transects (B and C) exhibit an average mixed layer depth of 3 and 5 m respectively (Fig. 8). The sections show that temperature changes are not limited to the surface
15   layer but reach about 40-50 m deep. While the temperature field in transect B exhibits a clear frontal structure, the isotherms are close to horizontal in transect C, with exception of undulations associated with internal waves propagating onshore (e.g. at km 46 in Fig. 8b). As a result, the mean cross-frontal velocity field shows no longer any clear offshore directed velocity signal (Fig. 7e). Also the subsurface along-frontal (poleward) velocity maximum of the PCUC appears to be weaker (Fig. 7f). During this last phase the outgassing of CO_2 is at its minimum with fluxes less than 20 mmol m^{-2} d^{-1} despite the again increased
20   wind speeds (Fig. 6d). fCO$_2$ remains at ∼600 μatm during this phase and increases only slightly along the last two transects during which the front starts to reform.

Figure 3 shows the correlation of surface temperature and $f\mathrm{CO_2}$ during the main experiment. The high negative correlation indicates the governing effect of temperature on the $\mathrm{CO_2}$ field. Especially during the beginning of the experiment the high $f\mathrm{CO_2}$ values are only found on the cold side of the front. Towards the end of the experiment the clear correlation signal breaks up. The changes in temperature and $f\mathrm{CO_2}$ are observed over the course of $\mathcal{O}$(hours), giving phytoplankton only a short time window to react. It is thus likely that physical processes are mainly responsible for the measured variability in surface $f\mathrm{CO_2}$. In the following part of this study, we analyze the observed changes across the upwelling front in the context of physical processes that could be responsible for driving the observed $f\mathrm{CO_2}$ variability.

4.1 Surface heat fluxes

The changes across the front are observed within a 24 hour period. The wind begins to drop at 11:00 on February 17 (06:00 local time) and the temperature gradient fully vanishes 14 hours later at 01:00 on February 18 (Fig. 6a). As this time period matches well with the diurnal cycle of solar insolation, it could be hypothesized that differential heating throughout the day causes the reduction of the cross-frontal temperature gradient. Figure 6f shows the diurnal cycle of net surface heat flux. During the zonal transects the ocean surface is heated on average by $50~\mathrm{W~m^{-2}}$. Due to the absence of solar insolation, this heatflux is mostly maintained by latent and sensible heat fluxes *into* the ocean, overcoming the ocean's weak heat loss caused by outgoing long wave radiation (individual heat flux components not shown). At around 12:00 (07:00 local time) the net heat flux into the ocean begins to strengthen, associated with an intensification of solar insolation. During the fourth and the beginning of the fifth cross-frontal transect the heat flux into the ocean is hampered due to irregularities in the incoming shortwave radiation. The net heat flux reaches its peak of $1010~\mathrm{W~m^{-2}}$ at 18:00 (13:00 local time) and reduces subsequently. From 23:00 (18:00 local time) onwards, the net heat flux fluctuates around $0~\mathrm{W~m^{-2}}$. During the last cross-frontal transects the surface is continuously cooled by less than $50~\mathrm{W~m^{-2}}$. During the phase of strongest heating, the heat flux shows only small lateral differences of mostly less than $50~\mathrm{W~m^{-2}}$ across the temperature front. Further, no clear pattern of slightly stronger heating on the cold side of the front is discernible. As a result, a uniform warming of the surface waters is expected. Sectional averaging of the first 13 cross-frontal transects, corresponding to the time period of incoming solar radiation, shows an increase of the transects' mean temperature of $0.8°\mathrm{C}$. From $\Delta Q = \rho_r c_p V \Delta T$ with the reference density $\rho_r = 1035~\mathrm{kgm^{-3}}$ and a heat capacity $c_p = 4000~\mathrm{Jkg^{-1}~m^{-3}}$ it can be roughly estimated that over the same time period of 14.5 hours the average net heat flux causes a warming of a surface water column of volume V with unit area and 10 m depth by $0.6°\mathrm{C}$. Thus, the background temperature increase is most likely linked to the surface heat fluxes. The small scale temperature anomalies develop during the phase of strong heating (Fig. 6b). Using the same calculation as above the maximum heatflux of $1010~\mathrm{W~m^{-2}}$ can warm the surface water by almost $0.1°\mathrm{C}$ per hour. Even though this roughly corresponds to the amplitude of the temperature anomalies, the lateral homogeneity of the net surface heat flux prohibits to attribute the development of the anomalies to surface heating.

The temperature front finally vanishes during a phase of almost no net surface heat flux. The high-resolution temperature transects B and C (Fig. 8) show, that during this phase, cooling takes place on the offshore side of the front, while the onshore side is significantly warmed over a period of 6 hours. On the onshore side, temperature changes of $\sim 2°\mathrm{C}$ occur up to ~ 40 m depth. A heatflux of $\sim 3800~\mathrm{W~m^{-2}}$ is required to heat a water column of 40 m by $0.5°\mathrm{C}$ using the rough estimate above.

Likewise, a comparably strong cooling is required on the offshore side of the front in order to explain the observed temperature changes. Neither the two heatfluxes nor the associated strong cross-frontal gradient are within the range of the observed values.

The net surface heat flux can be converted into a vertical buoyancy flux following $\langle w'b' \rangle_{Q_{net}} = \alpha g Q_{net}/(\rho c_p)$, where w' is the vertical velocity anomaly, b' is the buoyancy anomaly, g is the gravitational acceleration and α is the thermal expansion coefficient. Due to the lack of data, the calculation of the surface density ρ requires an assumption about the salinity. The initial CTD section shows a surface salinity varying between 35.1 and 35.2 (Fig. 5c). Thus, the surface water density ρ is calculated using a constant salinity of 35.1, yielding an uncertainty of density in the range of 0.1 kg m^{-3} and in vertical buoyancy fluxes of 1%. The mean values of $\langle w'b' \rangle_{Q_{net}}$ for each transect are shown in Fig. 9. During both, night and day time, the surface layer gains buoyancy. In the night this vertical buoyancy flux is weak, with a rate of less than 1×10^{-8} m^2 s^{-3}. During the day, vertical buoyancy fluxes of more than 5×10^{-7} m^2 s^{-3} act to stratify the surface layers.

While surface heat fluxes are shown to contribute to the overall evolution of the temperature field, they cannot explain the across-frontal variability. Especially, the observed temperature changes below the surface layer seem to be unconnected to surface heating. Thus, dynamical processes are investigated in the following to understand the reduction of the cross-frontal temperature gradient.

4.2 Ekman transport

Throughout the experiment the wind speed changed significantly from almost 12 m s^{-1} to 4 m s^{-1} , while the wind direction stayed almost parallel to the front in the same direction as the frontal jet, i.e. downfrontal (Fig. 4). The cross-frontal Ekman velocity is calculated as $u_{Ek} = \tau_0/(f \rho_0 H_{ML})$, where $\tau_0 = \rho_{air}\left(c_d u_{10}^2\right)$ is the neutral along-frontal surface wind stress. The drag coefficient c_d and the along-frontal wind speed at 10 m height u_{10} are calculated following Smith (1988). The mean density within the Ekman layer ρ_0 is approximated by the surface density ρ. Assuming a mixed layer depth H$_{ML} = 10$ m Ekman current velocities reach up to 0.5 m s^{-1} and are always directed offshore (figure not shown). During the period of the developing surface temperature anomalies, the Ekman velocity drops to ~ 0.1 m s^{-1}, agreeing with the observed cross-front velocities close to the surface (Fig. 7a,c). The large uncertainties in surface salinity lead to only minor errors in Ekman velocity of less than 10^{-3} m s^{-1}. The choice of the mixed layer depth has a far larger impact due to the inverse proportionality. For example choosing $H_{ML} = 5$ m leads to Ekman velocities larger by a factor of 2. The clear offshore direction of the Ekman transport is not affected by these uncertainties.

The wind driven Ekman transport is associated with a non-geostrophic overturning circulation in the vertical/cross-frontal plane (Thomas et al., 2008). For such an overturning circulation it is possible to infer the associated vertical buoyancy flux $\langle w'b' \rangle$. The Ekman buoyancy flux (EBF) is given by $\langle w'b' \rangle_{EBF} = \tau_0 \cdot \nabla b/(\rho_0 f)$ (Thomas and Lee, 2005), where f is the Coriolis parameter. ∇b is the cross-frontal buoyancy gradient, taken as the slope from a linear fit to the surface buoyancy across the front. Buoyancy is calculated as $b = -g(\rho - \rho_r)/\rho_r$ using a reference density $\rho_r = 1035$ kg m^{-3}.

Calculating the buoyancy gradient with a constant salinity value of 35.1 g kg^{-1} is likely to yield an error for the Ekman buoyancy fluxes as the initial CTD transect indicates a cross-fontal surface salinity gradient of -5×10^{-3} g kg^{-1} km^{-1}. Hence, this salinity gradient is imposed onto the mean value of 35.1 g kg^{-1} to estimate the cross-frontal buoyancy gradient. Figure

9 shows the buoyancy fluxes calculated for each transect. The EBF is enclosed by an uncertainty range related to the surface salinity gradient. The edges of this uncertainty range stem from the case of no cross-frontal salinity gradient and of double the initially observed cross-frontal gradient.

The downfrontal wind drives a continuous Ekman transport from the cold to the warm side of the front, thus acting to keep the isopycnals strongly tilted, rather than directly transporting warm water onshore. Correspondingly, the EBF is predominantly negative, signifying a destratification within the surface layer, inhibiting the slumping of isopycnals. During the cross-frontal transects, the EBF weakens drastically from -1×10^{-6} $\mathrm{m^2}$ $\mathrm{s^{-3}}$ to -2×10^{-7} $\mathrm{m^2}$ $\mathrm{s^{-3}}$. Only during cross-frontal transects 13-15 the buoyancy flux changes sign, which goes along with the turnaround of the surface temperature gradient (Fig. 6a) while the Ekman velocity continues to be directed offshore. Afterwards, during the reformation of the front towards the end of the experiment on February 18, the EBF returns to negative values.

The results above show, that the weakening of the temperature front is not directly caused by onshore Ekman transport. Still, the reduction in downfrontal (equatorward) wind speed and the associated weaking in offshore Ekman transport can change the frontal stability. During most of the experiment's duration, the EBF inhibited a slumping of isopynals. However, this flux weakened over the course of the experiment, potentially allowing other processes such as surface heat fluxes or mixed layer instabilities to become more important.

4.3 Mixed layer instabilities (MLIs)

Baroclinic instabilities confined to the mixed layer are referred to as submesoscale mixed layer instabilities (MLI) (Haine and Marshall, 1998; Boccaletti et al., 2007). They act to restratify the mixed layer by extracting potential energy from horizontal density gradients within the vertically well mixed surface layer and convert this into eddy kinetic energy, by formation of mixed layer eddies which accomplish the cross-frontal transport and exchange. With their short timescales of $\mathcal{O}(f^{-1})$ submesoscale MLI are thought to be efficient in converting lateral density fronts to a stratified mixed layer. Their horizontal scales are given by $L = NH_{ML}/f$, where $N = \sqrt{g/\rho\,(\partial\rho/\partial z)}$ is the small but non-vanishing stratification within the mixed layer (Thomas et al., 2008). Based on the initial CTD transect A (shown in Fig. 5) this lengthscale L is calculated to be 2.5 ± 1.5 km. The large error is accounting for the uncertainties in the mean mixed layer stratification, which is estimated to be $N \approx (6 \pm 4) \times 10^{-3}$ $\mathrm{s^{-1}}$. The inverse of the growth rate of MLI ($2\pi/f$) can be used as the associated timescale which amounts to ~ 2.1 days in the present case. The proximity of the study region to the equator associated with relatively long inertial timescales, makes it possible to capture well the variability by means of underway measurements.

Repeated observations of coherent surface temperature anomalies and their intensification between 15:00 and 20:00 on February 17 around 50 kilometers away from the coast might indicate the development of MLI (Fig. 6b). Preceeding their appearance are small anomalies in the current field averaged over the upper 40 m (Fig. 6e). There, the mostly southbound flow is reversing and weakly flowing northward, producing large relative vorticity values (cross-frontal transects 3, 4, 5). This points towards eddying structures which could be associated with MLI. The mixed layer depth, estimated by a $\Delta T = 0.2°\mathrm{C}$ criterion, shows a shallowing throughout the experiment. While the average mixed layer depth is 15 m during the CTD transect A it reduces to 3 and 5 m during transects B and C, respectively. We applied linear stability analysis, which provides vertical

11

modes of the growth of baroclinic instabilities (Brüggemann and Eden, 2014; Thomsen et al., 2014) to the laterally averaged stratification and geostrophic current shear profile from the intial CTD section (Fig. 10b,c). This analysis reveals the existance of both, a deep mesoscale mode and a shallow mode, confined to the mixed layer (Fig. 10a,d,e). The horizontal length scale of the deep mode is about 200 km, while it is only 8.7 km for the shallow mode. This length scale is of the same order of magnitude as the expected mixed layer deformation radius L and the size of the observed surface temperature anomalies. The initial growth rate of the shallow mode calculated from linear stability analysis is 0.5 day^{-1}. Once the instabilities grow too large, nonlinearities dominate the instability process and linear stability analysis may not provide a useful description of the evolution of the instabilities (Thomsen et al., 2014). However, the calculated growth rate is relatively slow compared to the observed rapid decline of the cross-frontal temperature gradient. Also the inferred shallow mode is limited to ~ 15 m depth, i.e. the mixed layer (Fig. 10e). Thus, instability-induced changes of the velocity field at 30 m depth would require an interaction with the deep mode (Fig. 10d).

Similar to Ekman dynamics, a secondary overturning circulation is driven by MLI. It is important to note, that while an EBF is associated with strong diapycnal mixing, pure mixed layer instabilities are of an adiabatic nature. According to Fox-Kemper et al. (2008) the vertical buoyancy flux due to MLI given by $\langle w'b' \rangle_{MLI} = CH_{ML}^2 (\nabla b)^2 / |f|$ (where $C = 0.08$ is a constant) always tends to reduce the lateral temperature gradient. Throughout the experiment the $\langle w'b' \rangle_{MLI}$ values are positive, indicating a restratification of the mixed layer. However, the buoyancy flux associated with MLI is in general about 10 times smaller than the EBF. During the stable front the buoyancy flux associated with MLI $\langle w'b' \rangle_{MLI}$ is less than 1×10^{-7} m^2 s^{-3} and reduces afterwards. Calculations are done with $H_{ML} = 15$ m based on the CTD transect. This is likely to be an upper bound for the mixed layer depth during the main experiment, as transects B and C show a much shallower mixed layer. Both linear stability analysis and buoyancy flux estimates imply that MLI are present, acting to restratify the mixed layer, but seem to be too slow and too confined to the surface layer, such that observed changes at depth cannot be explained by MLI alone.

4.4 Surface gravity current

In the presence of lateral density gradients, an unforced surface mixed layer is subject to pressure driven gravity currents, where lighter water spreads on top of the denser waters on timescales below the inertial period, i.e. independent of rotational effects (e.g. Kao et al. (1977)). The observed decrease in downfrontal wind speed could therefore give rise to the spreading of a buoyant plume down the temperature gradient. The rapid decline and even a slight reversal of the temperature front is captured well by transects B and C (Fig. 8). Within 6 hours the structure of both the temperature and cross-frontal velocity fields changed significantly. While transect B still shows a pronounced (subsurface) frontal signature, the isotherms in transect C are close to being horizontal. The temperature field in transect C is subject to distortion through internal waves. At km 46, the undulating isotherms go along with an oscillating signal in cross-front velocity, agreeing with internal waves propagating up the continental shelf. The strong depression of isotherms at km 57 could be the onset of another internal wave signal. In transect B, the temperature and velocity field exhibit a strong anomaly at km 52.5. There, a narrow but strong depression of the temperature field coincides with a region of strong convergence in the cross-frontal direction. Unlike in transect C, the attribution of the depression of the isotherms to an internal wave signal is not straightforward as the velocity field does not

12

show an oscillating behaviour in the vicinity of the depression. This might be attributed to aliasing of the signal due to too few hydrographic observations, which do not capture the short period of the internal waves.

Any density (here temperature) front is associated with a cross-frontal pressure gradient. In coastal upwelling regimes, this pressure gradient is largely in geostrophic balance manifesting itself in an along-frontal jet. However, if the wind field setting up the frontal system becomes too weak, the tilted isopycnals might start to slump, with the light surface waters offshore pushing over the denser surface water located further onshore. Thus, baroclinic temperature fronts can be eroded by gravity currents flowing down the pressure gradient across the front. Observations from river plumes show that the head of a gravity current may excite large-amplitude internal waves (Nash and Moum, 2005). These are either arrested at the leading edge of the gravity current or may propagate ahead of it if the current's advection speed is lower than that of the wave propagation speed. Assuming that the anomaly signals in transect B (at km 52.5) and C (at km 46) belong to the same internal wave package that propagates at the leading edge of the gravity current, a propagation speed of $0.4 \mathrm{~m~s}^{-1}$ is estimated using a time difference of 4.5 hours and a distance of 6.5 km. In a simple 2-layer model, the propagation speed of the gravity current in deep ambient fluid is given by $c = \sqrt{g'H}$, where $g' = g\Delta\rho/\rho$ is the reduced gravity, $\Delta\rho$ is the density difference between the two layers and H is the thickness of the upper layer (Shin et al., 2004; Dale et al., 2008). Assuming a 2-layer problem in the observed frontal setup with $H = 30$ m, as the average depth of the 15°C isotherm, and $g' = 5 \times 10^{-3} \mathrm{~m~s}^{-2}$ derived from densities calculated at 10 and 50 m depth, assuming a salinity of 35, the theoretical propagation speed c can be estimated to be $0.4 \mathrm{~m~s}^{-1}$, thus agreeing with the observed propagation speed. If the temperature anomalies in sections B and C represent an internal wave package propagating at the leading edge of a gravity current, the internal wave propagation speed estimates above qualify a density driven gravity current as a possible mechanism behind the abrupt degradation of the temperature front. In contrast to the other analyzed processes it is capable of explaining subsurface changes in the temperature field.

5   Comparison of buoyancy fluxes

Over the whole experiment, three of the four analyzed physical processes are comparable in terms of the associated vertical buoyancy fluxes (Fig. 9). The ratio

$$R_b = \frac{\langle w'b'\rangle_{Qnet>0} + \langle w'b'\rangle_{MLI} + \langle w'b'\rangle_{EBF>0}}{\langle w'b'\rangle_{Qnet<0} + \langle w'b'\rangle_{EBF<0}} \tag{1}$$

allows for a statement on the combined effect of the Ekman buoyancy flux, surface heating and MLI (Mahadevan et al., 2010; Taylor and Ferrari, 2011). The numerator only contains terms associated with stratification, i.e. positive buoyancy fluxes. For example the buoyancy flux associated with MLIs is always positive and thus appears only in the numerator. The EBF however changes sign during the experiment. During the parts of the experiment with positive EBF it will contribute to the term $\langle w'b'\rangle_{EBF>0}$ in the numerator. If the EBF is negative, its modulus will appear in the denominator as $\langle w'b'\rangle_{EBF<0}$. The same applies to the surface heating buoyancy fluxes. As a result, if $R_b > 1$, the mixed layer is subject to restratification associated with a slumping of isopycnals, whereas $R_b < 1$ implies a destratification, i.e. mixing in the surface layer. During the time of the development of the coherent surface temperature anomalies (cross-frontal transects 7-11), the combination of the

three processes favor a restratification of the mixed layer (Fig. 9). Linear stability analysis confirms the existance of a shallow baroclinic mode, which shows growth rates of $0.5 \, \mathrm{d}^{-1}$ on lengthscales of $8.7 \, \mathrm{km}$. The latter agrees well with the extent of the observed temperature anomalies and the mixed layer radius of deformation calculated from the initial CTD transect. While the temporal scale of the shallow mode is in agreement with the development of the surface temperature anomalies, its impact in the rapid decline of the temperature front around 00:00 on February 18 is probably low, as the growth rate at the initial phase of the instability seems too small. Further, the low associated buoyancy fluxes (Fig. 9) indicate that MLI may contribute only to a small degree to the observed change in the temperature gradient across the front.

In contrast, the buoyancy fluxes associated with surface heating and cross-frontal Ekman transport (Fig. 9) contribute to the changes in sign of the sum of the buoyancy flux (and to $R_b > 1$) during February 17. Even though the strength of the diabatic heating agrees well with the amplitude of the developing surface temperature anomaly, stronger than observed horizontal gradients in surface heating are required to induce the observed lateral differences in warming. Further, the nature of this buoyancy flux is purely vertical and thus unable to create horizontal gradients in the case of spatially uniform heating, opposed to buoyancy fluxes associated with MLI or Ekman dynamics, which are fully 3-dimensional.

The buoyancy flux related to a gravity current is mainly lateral. However, if the warm water spreads on top of the cold water on the onshore side of the front, a vertical buoyancy flux is induced. In a closed domain the mean vertical buoyancy flux can be estimated following $\partial E_p / \partial t \approx -\langle wb \rangle$ (Peltier and Caulfield, 2003; White and Helfrich, 2013), thus by comparing volume-averaged potential energies E_p at two different points in time t. In a 2-dimensional domain the volume-averaged potential energy is calculated as $E_p = (hd)^{-1} \int_d \int_0^h bz \, dz \, dx$, where d is the lateral distance and h is depth. Using a constant salinity value of 35 the buoyancy field is calculated for transects B and C. Considering the upper $70 \, \mathrm{m}$ on the initially cold side of the front (i.e. only east of 52 km offshore) a vertical buoyancy flux of $2.7 \times 10^{-6} \, \mathrm{m}^2 \, \mathrm{s}^{-3}$ is estimated. Laterally extending the domain to the full transects B and C reduces the vertical buoyancy flux to $1.8 \times 10^{-6} \, \mathrm{m}^2 \, \mathrm{s}^{-3}$. As the transects B and C have no closed boundaries, the estimates carry large uncertainties. The pressure driven gravity current is however assumed to be fully captured by both transects so that its associated effect should be captured. In the context of a closed domain the subsurface temperature reduction on the initialy warm side of the front could be associated with an upward suction of colder water balancing the downward pumping of surface water on the cold side of the front (Fig. 8).

The estimated flux due to the gravity current is much larger than the buoyancy fluxes associated with the other processes described above during the cross-frontal transects 12-14, regardless of the chosen cross-frontal width considered. Only the EBF during the beginning of the experiment is of the same order of magnitude.

6 Discussion

Gathering data from multiple ship surveys Friederich et al. (2008) observed oceanic outgassing of CO_2 in the Peruvian up-welling region throughout the year. On average the authors estimated a sea-to-air CO_2 flux of $5 \, \mathrm{mol} \, \mathrm{m}^{-2} \, \mathrm{yr}^{-1}$. On seasonal timescales, the flux varied between 2.5 and $10 \, \mathrm{mol} \, \mathrm{m}^{-2} \, \mathrm{yr}^{-1}$ associated with weak and strong upwelling periods, respectively. Although Friederich et al. (2008) focused on the large scale distribution of surface CO_2 fluxes and the associated mechanisms,

they further detected strong variability of CO_2 fluxes on short time and space scales ($\mathcal{O}$(hours-days) and $\mathcal{O}$(km)), which contributes significantly to the overall CO_2 budget.

Motivated by their findings, the study presented here focuses on the pronounced submesoscale variability of surface CO_2 in the Peruvian upwelling region at 13.7° S. Our observations show CO_2 outgassing rates between 3.5 and 30 mol m^{-2} yr^{-1} which are in line with the outgassing signals observed by Friederich et al. (2008), even after accounting for the difference in converting our values from partial pressures to fugacities (difference usually about 3%). Our peak sea-air fluxes reaching up to 80 mmol m^{-2} d^{-1} are distinctly higher than the maximum flux of 12.4 mmol m^{-2} d^{-1} reported by Friederich et al. (2008) for a measurement campaign in the month of February. At the same time, our peak-flux is only slightly higher than maximum flux values reported from other months. The results from Friederich et al. (2008) were re-scaled to a much larger area (5° S - 15° S), have been subject of spatial extrapolation and smoothing, and were calculated with the sea-air gas exchange parameterization by Wanninkhof (1992) which tends to overestimate the gas transfer velocities (see Wanninkhof (2014)). Simply using the Wanninkhof (1992) parameterization instead of the Nightingale et al. (2000) parameterization yields 17% higher fluxes, already indicating that it is difficult to draw a direct comparison between both data sets. Nonetheless, both studies agree in that the near-coastal zone off Peru acts as a rather strong source of CO_2 to the atmosphere, and from our data it seems clear that the onshore side of the upwelling front could be associated with an important enhancement of CO_2 outgassing. The conditions observed in this study are not necessarily representative for February conditions. Many processes on different timescales can alter the upwelling frontal structure and intensity off Peru, for instance the state of the El Niño Southern Oscillation (Espinoza-Morriberón et al., 2017) or coastally trapped waves propagating along the Peruvian coast (Pietri et al., 2014). The aim of this study is rather to analyze a suite of processes involved in the evolution of the upwelling front and surface fCO$_2$ on short space and timescales ($\mathcal{O}$(1 km), $\mathcal{O}$(0.5 day)).

The downfrontal wind is an important ingredient in maintaining tilted isopcynals in the surface layer. The EBF dominates all other buoyancy fluxes during the strong wind period (Fig. 9). In a study by Dale et al. (2008) a restratification of the mixed layer is observed in connection with a frontal decay in the upwelling system off Oregon on length scales comparable to those presented here. In their study, a reversal of the wind direction plays a crucial role in driving the frontal decay by inducing an Ekman transport down the cross-frontal pressure gradient. For the frontal decay presented here, the wind is always directed downfrontal and does not change significantly. The cross-frontal wind component is weak (mostly less than 3 m s^{-1}) and alternates in direction between onshore and offshore without any clear dominance (Fig. 4). As a result, Ekman transport and the associated buoyancy flux do not change direction. Still, the strong reduction in cross-frontal Ekman transport could potentially give way for other mechanisms.

Pronounced changes across the front are shown to occur in two steps after the distinct reduction in downfrontal wind speed with a time lag of about 9 hours. The first step is characterized by the gradual development and strengthening of coherent surface temperature anomalies, while the second is characterized by a sudden decline and even slight reversal of the temperaure gradient. Transects B and C (Fig. 8) show that changes in the temperature field are thereby not limited to the surface layer, but reach down to 50 m. To identify the underlying processes, the frontal evolution is described above in a 2-dimensional framework, i.e. in the vertical/cross-frontal plane. The variability induced by along-frontal advection is neglected. This assumption

15

seems valid, as the along-frontal current velocities reduce close to zero in proximity to the surface (Fig. 7b,d,e). Further, the fact that the cross-frontal transects show coherent signals, even though not all cross-frontal transects were performed on the exact same track, but about 1 km apart, points towards a weak along-frontal flow variability. Still, the two dimensional framework allows for various hypotheses about the driving mechanisms behind the observed changes.

5   The analyses have shown that the diurnal surface heating is able to explain the majority of the mean increase in surface temperatures. During the phase of maximum heating the associated positive buoyancy flux into the ocean outweighs the permanent reduction in surface buoyancy by the downfrontal wind stress (Fig. 9). However, the spatially homogeneous heating is unable to account for the developing small-scale temperatures anomalies. As a result, submesoscale MLI have been investigated as they are shown to restratify the surface mixed layer and are thereby capable of generating lateral gradients and anomalies.

10 Linear stability analysis indeed shows the presence of a shallow baroclinic mode confined to the mixed layer (Fig. 10). While the length scale of this mode roughly meets the observed horizontal extent of the temperature anomalies and the mixed layer deformation radius, the instability seems to grow too slowly to be the dominant dynamical process involved in the frontal decay. Hence, also the vertical buoyancy fluxes asociated with MLI are an order of magnitude smaller than those related to surface heating or Ekman dynamics (Fig. 9).

15   The low-latitude location of the experiment site at 13.77° S results in a rather long inertial time period of $T_{in} = 2\pi/f = 2.1$ days. Thus, the sudden changes observed from hydrographic sections B and C within a time span of 6 hours suggest that processes influenced by Earth's rotation, are potentially less important in the final weakening of the temperature front. Propagating buoyant plumes related to river discharge (Nash and Moum, 2005) or frontal zones in upwelling regimes (Walter et al., 2016) are common dynamical processes in continental shelf regions. In fact, Dale et al. (2008) also identified such

20 a pressure-driven gravity current propagating across the front, once the wind forcing had changed. For our case, using the limited amount of hydrographic information, a propagation speed of 0.4 m s^{-1} can be identified. This proves to match well with the theorectical estimate for a 2-layer system. The present stratification however complicates the distinction of a sharp density gradient to apply the gravity current theory. Further, stratified ambient water decreases the propagation speed of a gravity current compared to the two layer system (Ungarish and Huppert, 2002). Still, hinting towards the observation of a

25 gravity current, both transect B and C exhibit strong internal wave signals, which have been observed at the leading edge of such buoyant plumes (Nash and Moum (2005); Bourgault et al. (2016)). Of all mechanisms presented, the gravity current is the only one that may account for the fast changes up to 50 m depth. In contrast, the stability analysis suggests, that MLI are mainly active in the mixed layer and could only effect lower layers by interacting with the deep mode (Ramachandran et al., 2014; Capet et al., 2016).

30   In this study we set focus solely on the role of physical processes driving the small-scale distribution of $f\mathrm{CO_2}$. We argue that the timescales considered here are too short to allow for significant contributions of biological processes in driving $f\mathrm{CO_2}$ changes across the front. The strong correlation of surface temperature and $f\mathrm{CO_2}$ imply that the $f\mathrm{CO_2}$ variability is dominated by two processes: Firstly, the temperature dependent solubility of gases in seawater and secondly, warm offshore surface water pushing on top of $\mathrm{CO_2}$-enriched upwelled water, thus creating a mechanical barrier for air-sea gas exchange. However,

35 the weakening of the correlation over time (Fig. 3) indicates that other processes, such as biological activity, might become

increasingly important. A more thorough analysis from a biogeochemical perspective is needed, incorporating these effects (Mahadevan et al., 2004). Consistently, physical processes seem to be able to account for the small scale variability observed by Friederich et al. (2008) and understanding them could be crucial to establish a reliable CO_2 budget for the Peruvian upwelling region. Likewise, it is mandatory to have accurate observations of the near-shore wind field, as it proved to be an important factor that contributes to the small-scale evolution of the upwelling front. Modern satellite wind products are still too coarse to resolve the submesoscale frontal variability or other small scale variations such as land-sea breezes or an enhanced near-shore wind stress curl. They are thus not fully reliable within 25 to 50 km from shore (Croquette et al., 2007; Albert et al., 2010).

7   Conclusions

High-resolution, underway measurements are a useful tool in observing submesoscale variability on scales of $\mathcal{O}(1)$ km. Pronounced changes in the $f\text{CO}_2$ and temperature fields were observed across an upwelling front within hours, providing evidence of high short-term variability in the sea-air CO_2 exchange off Peru. We provide evidence of the complex submesoscale distribution of surface CO_2 in the Peruvian upwelling sytem and its tight connection to the strong variability in surface temperature. It thus appears that on these timescales the evolving $f\text{CO}_2$ distribution is controlled by physical processes.

Outgassing of CO_2 dropped from 80 $\mathrm{mmol\ m^{-2}\ d^{-1}}$ to less than 10 $\mathrm{mmol\ m^{-2}\ d^{-1}}$ within less than 24 hours. We showed that this drastic change can be explained by physical processes associated with a weakening of the cross-frontal temperature gradient following a significant decrease in downfrontal (equatorward) windspeed. The initially geostrophically balanced front with a length scale of 10 km vanished within few hours, thereby removing a surface temperature difference of 1°C over 10 km. Hydrographic data shows pronounced changes in the temperature field at depths of up to 50 m. Despite the lack of direct onshore transport of warm water by Ekman dynamics, the wind played a major role in maintaining the front in the beginning of the experiment. The decay of the downfrontal wind gave rise to the development of submesoscale mixed layer instabilities and potentially allowed for a gravity current to propagate down the cross-frontal pressure gradient. The mixed layer instabilities, however, appear to be too shallow and too slow to be able to account for the complete removal of the cross-frontal temperature gradient. Yet, the onset of a surface gravity current would be consistent with the observed changes in the subinertial period. In addition, our analysis shows that multiple processes act simultaneously and are likely to interact, thus complicating the identification of a single, dominant mechanism responsible for the fast observed changes in surface $f\text{CO}_2$.

At present, a low CO_2 data coverage within the Peruvian upwelling region (e.g. in SOCAT, Bakker et al. (2016)) complicates the establishment of a reliable climatology, as done by Takahashi et al. (2014) or more recently Landschützer et al. (2017). From our study the importance of the wind and temperature variability on timescales of $\mathcal{O}$(hours) in setting the strength of sea-air CO_2 fluxes becomes obvious. When coupled with CO_2 measurements the use of sea surface temperature and wind products, which capture the high temporal and spatial variability, could lead to improved future estimates of a CO_2 flux climatology off Peru. In order to understand the large scale impact of short-term variability of an upwelling ecosystem, a way forward would be the establishment of multi-platform observation networks in which continuous in situ data is complemented by satellite observations and measurements from autonomous platforms such as e.g. gliders, as for example conducted by Ohman et al.

(2013) in the California Current System. A further example are the moored CO_2 observations from Lefèvre et al. (2008) and Lefèvre and Merlivat (2012) which help to constrain regional budgets and variability of CO_2 for the Eastern Tropical Atlantic and could also be used to reliably estimate the net carbon community production in this area.

8 Data availability

5   According to the SFB 754 data policy (https://www.sfb754.de/de/data), all data associated with this publication are accessible upon publication under https://doi.pangaea.de/10.1594/PANGAEA.881049.

References

Albert, A., Echevin, V., Lévy, M., and Aumont, O.: Impact of nearshore wind stress curl on coastal circulation and primary productivity in the Peru upwelling system, Journal of Geophysical Research: Oceans, 115, C12 033, doi:10.1029/2010JC006569, 2010.

Arévalo-Martínez, D. L., Beyer, M., Krumbholz, M., Piller, I., Kock, A., Steinhoff, T., Körtzinger, A., and Bange, H. W.: A new method for continuous measurements of oceanic and atmospheric N_2O, CO and CO_2: performance of off-axis integrated cavity output spectroscopy (OA-ICOS) coupled to non-dispersive infrared detection (NDIR), Ocean Science, 9, 1071–1087, doi:10.5194/os-9-1071-2013, 2013.

Arévalo-Martínez, D. L., Kock, A., Löscher, C. R., Schmitz, R. A., and Bange, H. W.: Massive nitrous oxide emissions from the tropical South Pacific Ocean, Nature Geoscience, 8, 530–533, doi:10.1038/ngeo2469, 2015.

Bakker, D. C. E., Pfeil, B., Landa, C. S., Metzl, N., O'Brien, K. M., Olsen, A., Smith, K., Cosca, C., Harasawa, S., Jones, S. D., Nakaoka, S.-I., Nojiri, Y., Schuster, U., Steinhoff, T., Sweeney, C., Takahashi, T., Tilbrook, B., Wada, C., Wanninkhof, R., Alin, S. R., Balestrini, C. F., Barbero, L., Bates, N. R., Bianchi, A. A., Bonou, F., Boutin, J., Bozec, Y., Burger, E. F., Cai, W.-J., Castle, R. D., Chen, L., Chierici, M., Currie, K., Evans, W., Featherstone, C., Feely, R. A., Fransson, A., Goyet, C., Greenwood, N., Gregor, L., Hankin, S., Hardman-Mountford, N. J., Harlay, J., Hauck, J., Hoppema, M., Humphreys, M. P., Hunt, C. W., Huss, B., Ibánhez, J. S. P., Johannessen, T., Keeling, R., Kitidis, V., Körtzinger, A., Kozyr, A., Krasakopoulou, E., Kuwata, A., Landschützer, P., Lauvset, S. K., Lefèvre, N., Lo Monaco, C., Manke, A., Mathis, J. T., Merlivat, L., Millero, F. J., Monteiro, P. M. S., Munro, D. R., Murata, A., Newberger, T., Omar, A. M., Ono, T., Paterson, K., Pearce, D., Pierrot, D., Robbins, L. L., Saito, S., Salisbury, J., Schlitzer, R., Schneider, B., Schweitzer, R., Sieger, R., Skjelvan, I., Sullivan, K. F., Sutherland, S. C., Sutton, A. J., Tadokoro, K., Telszewski, M., Tuma, M., van Heuven, S. M. A. C., Vandemark, D., Ward, B., Watson, A. J., and Xu, S.: A multi-decade record of high-quality fCO_2 data in version 3 of the Surface Ocean CO_2 Atlas (SOCAT), Earth System Science Data, 8, 383–413, doi:10.5194/essd-8-383-2016, 2016.

Bentamy, A. and Fillon, D. C.: Gridded surface wind fields from Metop/ASCAT measurements, International Journal of Remote Sensing, 33, 1729–1754, doi:10.1080/01431161.2011.600348, 2012.

Boccaletti, G., Ferrari, R., and Fox-Kemper, B.: Mixed Layer Instabilities and Restratification, Journal of Physical Oceanography, 37, 2228–2250, doi:10.1175/JPO3101.1, 2007.

Bourgault, D., Galbraith, P. S., and Chavanne, C. P.: Generation of internal solitary waves by frontally forced intrusions in geophysical flows, Nature Communications, 7, 13 606, doi:10.1038/ncomms13606, 2016.

Brüggemann, N. and Eden, C.: Evaluating Different Parameterizations for Mixed Layer Eddy Fluxes induced by Baroclinic Instability, Journal of Physical Oceanography, 44, 2524–2546, doi:10.1175/JPO-D-13-0235.1, 2014.

Capet, X., Roullet, G., Klein, P., and Maze, G.: Intensification of Upper-Ocean Submesoscale Turbulence through Charney Baroclinic Instability, Journal of Physical Oceanography, 46, 3365–3384, doi:10.1175/JPO-D-16-0050.1, 2016.

Capone, D. G. and Hutchins, D. A.: Microbial biogeochemistry of coastal upwelling regimes in a changing ocean, Nature Geoscience, 6, 711–717, doi:10.1038/ngeo1916, 2013.

Chaigneau, A., Gizolme, A., and Grados, C.: Mesoscale eddies off Peru in altimeter records: Identification algorithms and eddy spatio-temporal patterns, Progress in Oceanography, 79, 106–119, doi:10.1016/j.pocean.2008.10.013, 2008.

Chavez, F. P., Takahashi, T., Cai, W.-J., Friederich, G., Hales, B., Wanninkhof, R., and Feely, R.: Coastal oceans, in: The First State of the Carbon Cycle Report (SOCCR): The North American Carbon Budget and Implications for the Global Carbon Cycle, edited by King, A. W., Dilling, L., Zimmerman, G. P., Fairman, D. M., Houghton, R. A., Marland, G., Rose, A. Z., and Wilbanks, T. J., A report by the U.S. Climate Change Science Program and the Subcommittee on Global Change Research, Washington, DC, 2007.

Colas, F., McWilliams, J. C., Capet, X., and Kurian, J.: Heat balance and eddies in the Peru-Chile current system, Climate Dynamics, 39, 509–529, doi:10.1007/s00382-011-1170-6, 2012.

Croquette, M., Eldin, G., Grados, C., and Tamayo, M.: On differences in satellite wind products and their effects in estimating coastal upwelling processes in the south-east Pacific, Geophysical Research Letters, 34, L11 608, doi:10.1029/2006GL027538, 2007.

5 Dale, A. C., Barth, J. A., Levine, M. D., and Austin, J. A.: Observations of mixed layer restratification by onshore surface transport following wind reversal in a coastal upwelling region, Journal of Geophysical Research: Oceans, 113, C01 010, doi:10.1029/2007JC004128, 2008.

Dickson, A. G., Sabine, C. L., and Christian, J. R., eds.: Guide to best practices for ocean CO_2 measurements. PICES Special Publication 3, 191 pp., 2007.

Espinoza-Morriberón, D., Echevin, V., Colas, F., Tam, J., Ledesma, J., Vásquez, L., and Graco, M.: Impacts of El Niño events on the Peruvian

10 upwelling system productivity, Journal of Geophysical Research: Oceans, 122, 5423–5444, doi:10.1002/2016JC012439, 2017.

Fairall, C. W., Bradley, E. F., Godfrey, J. S., Wick, G. A., Edson, J. B., and Young, G. S.: Cool-skin and warm-layer effects on sea surface temperature, Journal of Geophysical Research: Oceans, 101, 1295–1308, doi:10.1029/95JC03190, 1996a.

Fairall, C. W., Bradley, E. F., Rogers, D. P., Edson, J. B., and Young, G. S.: Bulk parameterization of air-sea fluxes for Tropical Ocean-Global Atmosphere Coupled-Ocean Atmosphere Response Experiment, Journal of Geophysical Research: Oceans, 101(C2), 3747–3764,

15 doi:10.1029/95JC03205, 1996b.

Ferrari, R.: A frontal challenge for climate models., Science, 332, 316–317, doi:10.1126/science.1203632, 2011.

Fox-Kemper, B., Ferrari, R., and Hallberg, R.: Parameterization of Mixed Layer Eddies. Part I: Theory and Diagnosis, Journal of Physical Oceanography, 38, 1145–1165, doi:10.1175/2007JPO3792.1, 2008.

Friederich, G. E., Ledesma, J., Ulloa, O., and Chavez, F. P.: Air-sea carbon dioxide fluxes in the coastal southeastern tropical Pacific, Progress

20 in Oceanography, 79(2-4), 156–166, doi:10.1016/j.pocean.2008.10.001, 2008.

Gruber, N.: Ocean biogeochemistry: Carbon at the coastal interface, Nature, 517, 148–149, doi:10.1038/nature14082, 2015.

Haine, T. W. N. and Marshall, J.: Gravitational, Symmetric, and Baroclinic Instability of the Ocean Mixed Layer, Journal of Physical Oceanography, 28, 634–658, doi:10.1175/1520-0485(1998)028<0634:GSABIO>2.0.CO;2, 1998.

Kao, T. W., Park, C., and Pao, H.-P.: Buoyant surface discharge and small-scale oceanic fronts: A numerical study, Journal of Geophysical

25 Research, 82, 1747–1752, doi:10.1029/JC082i012p01747, 1977.

Körtzinger, A., Mintrop, L., Wallace, D. W., Johnson, K. M., Neill, C., Tilbrook, B., Towler, P., Inoue, H. Y., Ishii, M., Shaffer, G., et al.: The international at-sea intercomparison of $f CO_2$ systems during the R/V Meteor Cruise 36/1 in the North Atlantic Ocean, Marine Chemistry, 72, 171–192, 2000.

Landschützer, P., Gruber, N., and C. E. Bakker, D.: An updated observation-based global monthly gridded sea surface pCO$_2$ and air-sea CO$_2$

30 flux product from 1982 through 2015 and its monthly climatology (NCEI Accession 0160558). Version 2.2. NOAA National Centers for Environmental Information. Dataset. [2017-07-11], 2017.

Lapeyre, G. and Klein, P.: Impact of the small-scale elongated filaments on the oceanic vertical pump, Journal of Marine Research, 64, 835–851, doi:10.1357/002224006779698369, 2006.

Laruelle, G. G., Lauerwald, R., Pfeil, B., and Regnier, P.: Regionalized global budget of the CO$_2$ exchange at the air-water interface in

35 continental shelf seas, Global Biogeochemical Cycles, 28, 1199–1214, doi:10.1002/2014GB004832, 2014.

Lefèvre, N. and Merlivat, L.: Carbon and oxygen net community production in the eastern tropical Atlantic estimated from a moored buoy, Global biogeochemical cycles, 26, 2012.

Lefèvre, N., Guillot, A., Beaumont, L., and Danguy, T.: Variability of fCO$_2$ in the Eastern Tropical Atlantic from a moored buoy, Journal of Geophysical Research: Oceans, 113, 2008.

Lévy, M., Ferrari, R., Franks, P. J. S., Martin, A. P., and Rivière, P.: Bringing physics to life at the submesoscale, Geophysical Research Letters, 39, doi:10.1029/2012GL052756, 2012.

5 Loginova, A. N., Thomsen, S., and Engel, A.: Chromophoric and fluorescent dissolved organic matter in and above the oxygen minimum zone off Peru, Journal of Geophysical Research: Oceans, 121, 7973–7990, doi:10.1002/2016JC011906, 2016.

Mahadevan, A., Lévy, M., and Mémery, L.: Mesoscale variability of sea surface pCO$_2$: What does it respond to?, Global Biogeochemical Cycles, 18, GB1017, doi:10.1029/2003GB002102, 2004.

Mahadevan, A., Tandon, A., and Ferrari, R.: Rapid changes in mixed layer stratification driven by submesoscale instabilities and winds,
10 Journal of Geophysical Research, 115, C03 017, doi:10.1029/2008JC005203, 2010.

McWilliams, J. C., Colas, F., and Molemaker, M. J.: Cold filamentary intensification and oceanic surface convergence lines, Geophysical Research Letters, 36, L18 602, doi:10.1029/2009GL039402, 2009.

Merlivat, L., Gonzalez Davila, M., Caniaux, G., Boutin, J., and Reverdin, G.: Mesoscale and diel to monthly variability of CO$_2$ and carbon fluxes at the ocean surface in the northeastern Atlantic, Journal of Geophysical Research, 114, C03 010, doi:10.1029/2007JC004657,
15 2009.

Meyer, J., Löscher, C. R., Lavik, G., and Riebesell, U.: Mechanisms of P* Reduction in the Eastern Tropical South Pacific, Frontiers in Marine Science, 4, 1, doi:10.3389/fmars.2017.00001, 2017.

Nash, J. D. and Moum, J. N.: River plumes as a source of large-amplitude internal waves in the coastal ocean, Nature, 437, 400–403, doi:10.1038/nature03936, 2005.

20 Nightingale, P. D., Malin, G., Law, C. S., Watson, A. J., Liss, P. S., Liddicoat, M. I., Boutin, J., and Upstill-Goddard, R. C.: In situ evaluation of air-sea gas exchange parameterizations using novel conservative and volatile tracers, Global Biogeochemical Cycles, 14(1), 373–387, doi:10.1029/1999GB900091, 2000.

Ohman, M. D., Rudnick, D. L., Chekalyuk, A., Davis, R. E., Feely, R. A., Kahru, M., Jim, H.-J., Landry, M. R., Martz, T. R., Sabine, C. L., and Send, U.: Autonomous ocean measurements in the California Current Ecosystem, Oceanography, 26, 18–25, 2013.

25 Payne, R. E.: Albedo of the Sea Surface, Journal of the Atmospheric Sciences, 29, 959–970, doi:10.1175/1520-0469(1972)029<0959:AOTSS>2.0.CO;2, 1972.

Peltier, W. R. and Caulfield, C. P.: Mixing efficiency in stratified shear flows, Annual Review of Fluid Mechanics, 35, 135–167, doi:10.1146/annurev.fluid.35.101101.161144, 2003.

Penven, P., Echevin, V., Pasapera, J., Colas, F., and Tam, J.: Average circulation, seasonal cycle, and mesoscale dynamics of the Peru Current
30 System: A modeling approach, Journal of Geophysical Research, 110, C10 021, doi:10.1029/2005JC002945, 2005.

Pierrot, D., Neill, C., Sullivan, K., Castle, R., Wanninkhof, R., Lüger, H., Johannessen, T., Olsen, A., Feely, R. A., and Cosca, C. E.: Recommendations for autonomous underway pCO$_2$ measuring systems and data-reduction routines, Deep Sea Research Part II: Topical Studies in Oceanography, 56, 512–522, 2009.

Pietri, A., Echevin, V., Testor, P., Chaigneau, A., Mortier, L., Grados, C., and Albert, A.: Impact of a coastal-trapped wave on the near-coastal
35 circulation of the Peru upwelling system from glider data, Journal of Geophysical Research: Oceans, 119, 2109–2120, 2014.

Ramachandran, S., Tandon, A., and Mahadevan, A.: Enhancement in vertical fluxes at a front by mesoscale-submesoscale coupling, Journal of Geophysical Research: Oceans, 119, 8495–8511, doi:10.1002/2014JC010211, 2014.

Resplandy, L., Lévy, M., D'Ovidio, F., and Merlivat, L.: Impact of submesoscale variability in estimating the air-sea CO_2 exchange: Results from a model study of the POMME experiment, Global Biogeochemical Cycles, 23, GB1017, doi:10.1029/2008GB003239, 2009.

Rudnick, D. L.: On the skewness of vorticity in the upper ocean, Geophysical Research Letters, 28(10), 2045–2048, doi:10.1029/2000GL012265, 2001.

5 Shin, J., Dalziel, S., and Linden, P.: Gravity currents produced by lock exchange, Journal of Fluid Mechanics, 521, 1–34, 2004.

Smith, S. D.: Coefficients for sea surface wind stress, heat flux, and wind profiles as a function of wind speed and temperature, Journal of Geophysical Research: Oceans, 93(C12), 15 467–15 472, doi:10.1029/JC093iC12p15467, 1988.

Takahashi, T., Sutherland, S. C., Wanninkhof, R., Sweeney, C., Feely, R. A., Chipman, D. W., Hales, B., Friederich, G., Chavez, F., Sabine, C., Watson, A., Bakker, D. C., Schuster, U., Metzl, N., Yoshikawa-Inoue, H., Ishii, M., Midorikawa, T., Nojiri, Y., Körtzinger, A., Steinhoff,

10 T., Hoppema, M., Olafsson, J., Arnarson, T. S., Tilbrook, B., Johannessen, T., Olsen, A., Bellerby, R., Wong, C., Delille, B., Bates, N., and de Baar, H. J.: Climatological mean and decadal change in surface ocean pCO_2, and net sea–air CO_2 flux over the global oceans, Deep Sea Research Part II, 56, 554 – 577, doi:10.1016/j.dsr2.2008.12.009, 2009.

Takahashi, T., Sutherland, S. C., Chipman, D. W., Goddard, J. G., Newberger, T., and Sweeney, C.: Climatological distributions of pH, pCO_2, total CO_2, alkalinity, and $CaCO_3$ saturation in the global surface ocean. ORNL/CDIAC-160, NDP-094., Carbon Dioxide Information

15 Analysis Center, Oak Ridge National Laboratory, U.S. Department of Energy, Oak Ridge, Tennessee, doi:10.3334/CDIAC/OTG.NDP094, 2014.

Taylor, J. R. and Ferrari, R.: Ocean fronts trigger high latitude phytoplankton blooms, Geophysical Research Letters, 38, L23 601, doi:10.1029/2011GL049312, 2011.

Thomas, L. N. and Lee, C. M.: Intensification of Ocean Fronts by Down-Front Winds, Journal of Physical Oceanography, 35, 1086–1102,

20 doi:10.1175/JPO2737.1, 2005.

Thomas, L. N., Tandon, A., and Mahadevan, A.: Submesoscale Processes and Dynamics, in: Ocean Modeling in an Eddying Regime, edited by Hecht, M. W. and Hasumi, H., American Geophysical Union, Washington, D. C., doi:10.1029/177GM04, 2008.

Thomsen, S., Eden, C., and Czeschel, L.: Stability Analysis of the Labrador Current, Journal of Physical Oceanography, 44, 445–463, doi:10.1175/JPO-D-13-0121.1, 2014.

25 Thomsen, S., Kanzow, T., Colas, F., Echevin, V., Krahmann, G., and Engel, A.: Do submesoscale frontal processes ventilate the oxygen minimum zone off Peru?, Geophysical Research Letters, 43, 8133–8142, doi:10.1002/2016GL070548, 2016a.

Thomsen, S., Kanzow, T., Krahmann, G., Greatbatch, R. J., Dengler, M., and Lavik, G.: The formation of a subsurface anticyclonic eddy in the Peru-Chile Undercurrent and its impact on the near-coastal salinity, oxygen, and nutrient distributions, Journal of Geophysical Research: Oceans, 121, 476–501, doi:10.1002/2015JC010878, 2016b.

30 Ungarish, M. and Huppert, H. E.: On gravity currents propagating at the base of a stratified ambient, Journal of Fluid Mechanics, 458, 283–301, doi:10.1017/S0022112002007978, 2002.

Walter, R. K., Stastna, M., Woodson, C. B., and Monismith, S. G.: Observations of nonlinear internal waves at a persistent coastal upwelling front, Continental Shelf Research, 117, 100–117, doi:10.1016/j.csr.2016.02.007, 2016.

Wanninkhof, R.: Relationship between wind speed and gas exchange over the ocean, Journal of Geophysical Research: Oceans, 97, 7373–

35 7382, doi:10.1029/92JC00188, 1992.

Wanninkhof, R.: Relationship between wind speed and gas exchange over the ocean revisited, Limnology and Oceanography: Methods, 12, 351–362, doi:10.4319/lom.2014.12.351, 2014.

Weiss, R. F.: Carbon dioxide in water and seawater: the solubility of a non-ideal gas, Marine Chemistry, 2, 203–215, doi:10.1016/0304-4203(74)90015-2, 1974.

Weiss, R. F. and Price, B. A.: Nitrous oxide solubility in water and seawater, Marine Chemistry, 8, 347–359, doi:10.1016/0304-4203(80)90024-9, 1980.

5   White, B. L. and Helfrich, K. R.: Rapid gravitational adjustment of horizontal shear flows, Journal of Fluid Mechanics, 721, 86–117, doi:10.1017/jfm.2013.41, 2013.
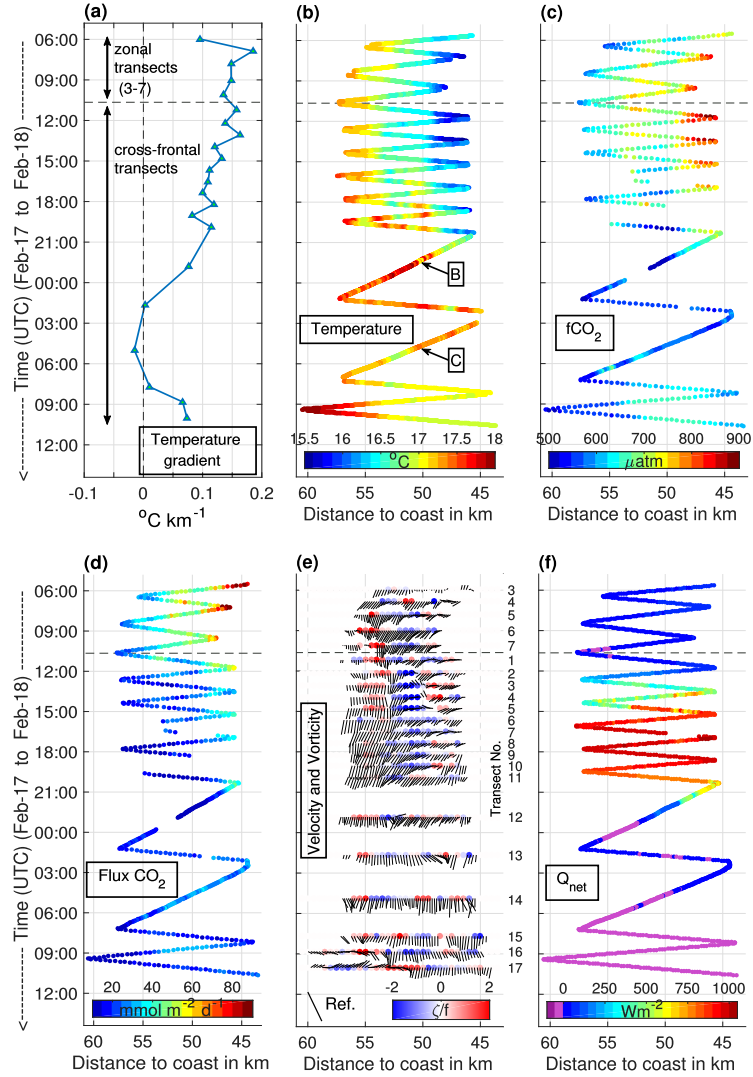
Figure 6. Hovmoeller diagrams of the cross-frontal surface temperature gradient (a), underway surface temperatures (b), surface fCO$_2$ (c), ocean-atmosphere CO$_2$ fluxes (d), mean current velocities in the upper 40 m (black lines) and vorticity (colored circles) (e) and diabatic surface heating (f) for the last five zonal transects and the subsequent 17 cross-frontal transects. The horizontal dashed line indicates the transition from zonal transects to repeated cross-frontal transects. Temperature gradients in (a) are calculated using a linear fit to the surface temperature transect shown in (b). In (b) the position of transects B and C is indicated. The vorticity of the vertically averaged velocity in (e) is calculated as $\zeta = \partial u_{al}/\partial y$ (Rudnick, 2001), where u_{al} is the along-front velocity and y is the cross-frontal distance, taken to be 2 km, comparable to the mixed layer deformation radius. The reference arrow in the bottom left corner anchored at 60 km from the coast indicates a flow with 0.3 m s^{-1} in the onshore (cross-front) and 0.3 m s^{-1} in the poleward along-front direction. The vorticity is normalized by the Coriolis parameter to give a proxy for the Rossby number. Velocity and vorticity are plotted at the time mean for each transect. Time is given in UTC.
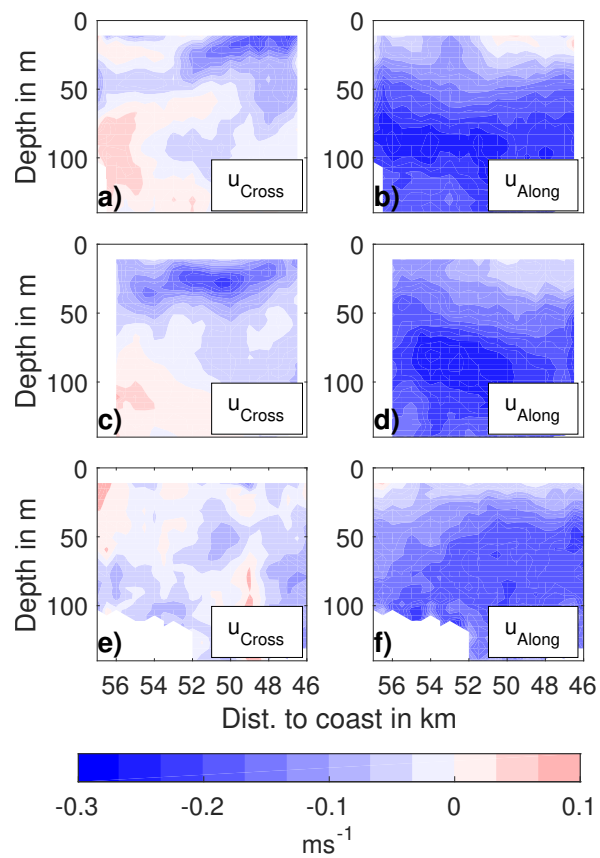
24

Figure 7. Mean cross- and along-front current velocities for cross-frontal trasects 1-6 in (a) and (b), 7-11 in (c) and (d) and 12-17 in (e) and (f). Currents are horizonatally binned onto a 500 m grid and subsequently averaged.
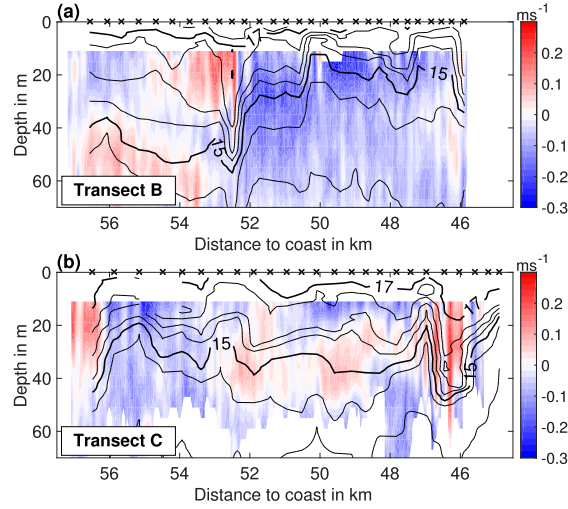
Figure 8. Temperature (black contour lines) and cross-front velocity (color-coded) for Transects B (a) and C (b) conducted as the 12th and 14th cross-frontal transect, starting on February 17 21:00 and February 18 03:00, respectively. Black crosses show the location of the temperature profiles from the microstructure probe. For both transects the ship moved away from the coast (right to left).
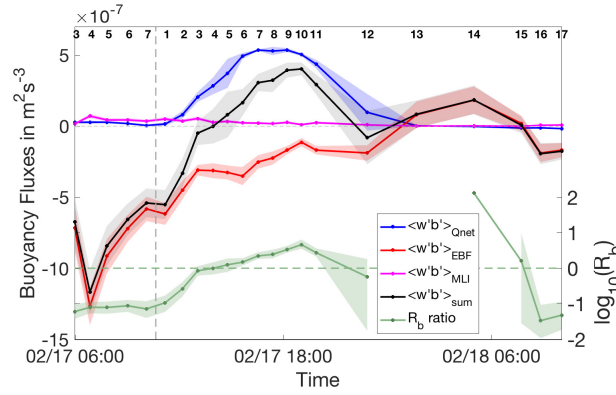

Figure 9. Vertical buoyancy fluxes associated with surface heating (blue), Ekman transport (red) and mixed layer instabilities (magenta). The shaded areas around the Ekman buoyancy flux (EBF) and the buoyancy flux associated with mixed layer instabilities (MLI) are accounting for uncertainties in the surface salinity gradient (see text for more details). The shaded uncertainty range for vertical buoyancy fluxes due to surface heating is given as one standard deviation obtained from sectional averaging. The sum of the three processes is given by the black line. The uncertainty is given as the maximum error resulting from the three processes. The R_b ratio (green) and its uncertainty are treated similarly. For cross-frontal transect 13 and 14 no R_b value or error can be stated due to the vanishing denominator in the definition of R_b. $\log_{10}(R_b) > 0$ points towards a net restratification, while $\log_{10}(R_b) < 0$ indicates a destabilization of the water column. For calculation details of all quantities see text. Time is given in UTC. The small black numbers on top indicate the respective zonal or cross-frontal transect number.
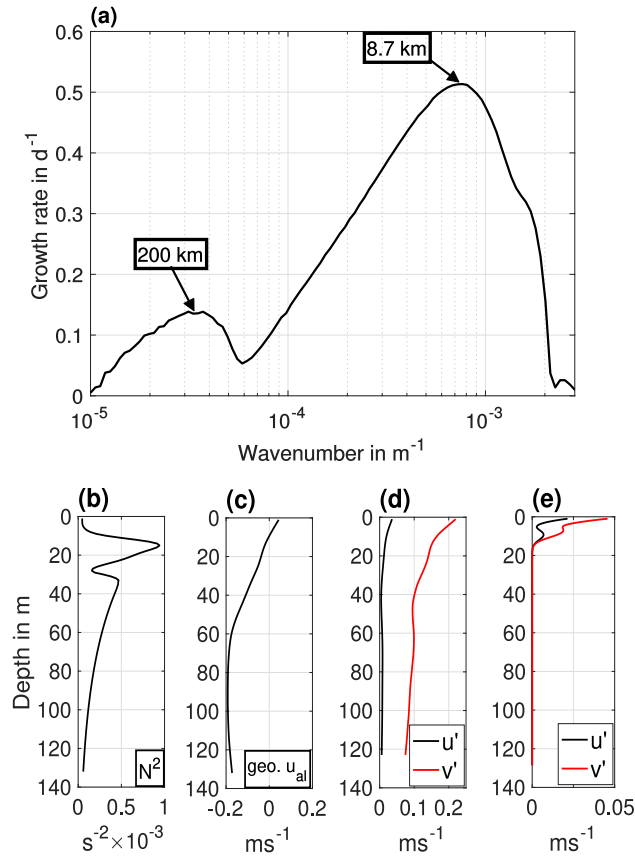
Figure 10. (a) Initial growth rate of barolinic instabilities obtained from linear stability analysis, applied to the frontal state during the CTD section (transect A). The local maxima of the growth rate are labeled by their corresponding length scale in km. The smoothed stratification and geostrophic along-frontal velcity profiles used as the background state, are shown in panels (b) and (c). A deep mode at large horizontal scales (200 km) and a shallow mode, associated with mixed layer instabilities and short horizontal length scales (8.7 km) are present. The corresponding anomalies for the cross-front (u) and along-front (v) velocities are shown in panels (d) and (e) for the deep and shallow modes, respectively.